Cell Research

www.nature.com/cr
www.cell-research.com

ARTICLE

Asymmetric division in a two-cell-like state rejuvenates embryonic stem cells

Xinyi Wang[1,2,9], Hong Fu[2,3,9], Qingyang Sun[2,3,4,9], Boyan Huang[1,2,9], Zhe Xu[1,2,9], Xuzhao Zhai[2,5], Chuncao Deng[2,6], Laru Peng[1,2], Mengdan Zhang[1,2], Tianran Peng[1,2], An Gong[1,2], Jiasui Liu[1,2,8], Zhengzhi Zou[4], Guangjin Pan[7], Jiekai Chen[7], Guangming Wu[2], Man Zhang[1,2]✉ and Mingwei Min[1,2]✉

A fundamental question in biology is whether all cells age. Embryonic stem cells (ESCs) defy the norm as rare normal cells capable of indefinite in vitro passage. However, the mechanisms underlying ESC lineage immortality remain unresolved. Using long-term live-cell imaging to follow the fates of single ESCs, we show that ESC lineage renewal is achieved through sporadic entry into a state characterized by the expression of two-cell embryo-specific markers. During this state, cells undergo asymmetric fate divisions, enriching accumulated DNA damage into one daughter lineage that is destined for elimination, while producing a second lineage that reverts to the pluripotent state. Importantly, the latter lineage exhibits signs of rejuvenation, including reduced DNA damage and enhanced chimeric efficiency. These findings underscore the crucial role of asymmetric cell division in maintaining the long-term health of the ESC lineage against mounting damage within individual cells and provide a potential model for studying cellular aging and rejuvenation in mammalian cells.

Cell Research (2026) 0:1–14; https://doi.org/10.1038/s41422-026-01221-z

INTRODUCTION

The lineage of all life today traces back to an ancestor 3.8 billion years ago. Although the overall life lineage appears to be immortal, individual organisms succumb to aging and mortality. This duality is often attributed to the division of labor between germline and soma. In this framework, the germline perpetuates the lineage, whereas the soma accumulates damage and is ultimately disposable.[1,2] Most somatic cells exhibit progressive functional decline during proliferation — a phenomenon classically attributed to telomere attrition, DNA damage, and epigenetic drift.[3] Embryonic stem cells (ESCs), however, defy this trajectory, achieving lineage immortality through indefinite in vitro proliferation while maintaining their function, a long-sought property in regenerative medicine. Specifically, these long-term passaged ESCs maintain a normal karyotype and the capacity to contribute to chimeric animals.[4,5] Although mechanisms of telomere maintenance in ESCs are well characterized,[6–8] it remains unclear how these cells evade the cumulative burden of molecular damage that limits the lifespan of other cell types.

A clue lies in the transient activation of programs associated with the two-cell (2C) embryo stage. ESCs occasionally enter a 2C-like state marked by the expression of genes such as MERVL and *Zscan4*.[6,9] Intriguingly, knockdown of *Zscan4* or depletion of MERVL-expressing cells induces a culture crisis of ESCs,[6,10] whereas overexpression of *Zscan4* enhances pluripotency,[11] suggesting that the spontaneous 2C-like state may serve as a 'fountain of youth' for the ESC lineage. Paradoxically, 2C-like cells exhibit increased replication stress, DNA damage, and apoptosis,[12–16] underscoring a gap in our understanding of how the transient 2C-like state might contribute to long-term lineage renewal of ESCs.

We propose two non-exclusive hypotheses: 2C-like cells either employ unusually efficient biochemical repair mechanisms to counteract cellular aging, or sort away damaged components. Using long-term live-cell imaging, we tracked the fate and damage status of individual ESCs spontaneously entering the 2C-like state. Our data support the latter hypothesis. Upon entering the 2C-like state, cells undergo asymmetric divisions, producing two distinct progenies: one lineage is enriched in damaged DNA and prone to cell death, while the other reacquires pluripotency with reduced damage. Functional assays confirm that the latter lineage makes an enhanced chimeric contribution to developing embryos, whereas blocking entry into the 2C-like state compromises ESC self-renewal. These findings position asymmetric division within the 2C-like state as a critical quality-control mechanism, enabling ESCs to sustain lineage immortality despite spontaneous DNA damage.

---

[1]GMU-GIBH Joint School of Life Sciences, The Guangdong-Hong Kong-Macao Joint Laboratory for Cell Fate Regulation and Diseases, Guangzhou Medical University, Guangzhou, Guangdong, China. [2]Guangzhou National Laboratory, Guangzhou, Guangdong, China. [3]School of Life Science and Technology, ShanghaiTech University, Shanghai, China. [4]MOE Key Laboratory of Laser Life Science and Institute of Laser Life Science, College of Biophotonics, South China Normal University, Guangzhou, Guangdong, China. [5]Zhongshan School of Medicine, Sun Yat-Sen University, Guangzhou, Guangdong, China. [6]Department of Biomedical Engineering, College of Life Science and Technology, Huazhong University of Science and Technology, Wuhan, Hubei, China. [7]Guangzhou Institutes of Biomedicine and Health, Chinese Academy of Sciences, Guangzhou, Guangdong, China. [8]Present address: Department of Molecular Sociology, Max Planck Institute of Biophysics, Frankfurt am Main, Germany. [9]These authors contributed equally: Xinyi Wang, Hong Fu, Qingyang Sun, Boyan Huang, Zhe Xu. ✉email: zhang_man@gzlab.ac.cn; min_mingwei@gzlab.ac.cn

Received: 12 May 2025 Accepted: 13 January 2026

RESULTS

2C-like cells undergo asymmetric divisions

To trace the fate of 2C-like cells, we established a mouse embryonic stem cell (mESC) line expressing a MERVL promoter-driven GFP reporter (MERVL::GFP) to mark the 2C-like state[9] and H2B-mIFP to track cells.[17] The MERVL::GFP signal strongly correlated with staining of endogenous MERVL-Gag protein, a capsid protein produced when the MERVL genetic sequence is activated (Supplementary information, Fig. S1a). Using time-lapse imaging, we followed the lineages of cells entering the 2C-like state (Fig. 1a). Surprisingly, cells that displayed a strong MERVL::GFP signal predominantly underwent cell death (Fig. 1b, c; Supplementary information, Fig. S1b and Video S1). Since control cells expressing CAG::GFP did not die (Supplementary information, Video S2), these results directly link cell death to the 2C-like state. This observation appears contrary to the hypothesis that the 2C-like state promotes the renewal of mESCs.

Quantification of lineage survival revealed that ~40% of the MERVL::GFP$^+$ cells died within 72 h (Fig. 1d). The remaining living MERVL::GFP$^+$ cells exhibited diminished GFP intensity (Fig. 1e, f) and progressively transitioned into a MERVL::GFP$^-$ state within a few generations (Supplementary information, Video S3). We denote these two fates as 2C-death and 2C-survived, respectively. Although only 1% of mESCs are in the MERVL::GFP$^+$ state at any moment, about 60% of mESCs are derived from the 2C-survived lineages by the end of the 4-day movie (Supplementary information, Fig. S1c).

Are the 2C-death and 2C-survived fates independent or interconnected? Upon entering the MERVL::GFP$^+$ state, about 30% of cells generated only the 2C-death fate, whereas 10% generated only the 2C-survived fate. The 2C-survived-only cells generally expressed very low levels of the 2C reporter, suggesting that their 2C-like program is not fully active. About 60% of cells gave rise to two daughter cells with distinct lineage fates: one 2C-death and the other 2C-survived (Fig. 1f–h; Supplementary information, Fig. S1d and Video S3). The prevalence of coupled cell fates far exceeds that expected by random chance: Given that approximately 1% of mESCs are MERVL$^+$ at any given time,[9] the probability of a cell generating the 2C-survived or 2C-death fate can be derived as $P(\text{2C-survived}) = 1\% \times (0.1 + 0.6) = 7 \times 10^{-3}$ and $P(\text{2C-death}) = 1\% \times (0.3 + 0.6) = 9 \times 10^{-3}$. If the two fates are independent, the chance of them occurring in the same lineage would be $P(\text{2C-survived}) \times P(\text{2C-death}) = 6.3 \times 10^{-5}$, two orders of magnitude less than the observed probability $P(\text{2C-survived, 2C-death}) = 1\% \times 0.6 = 6 \times 10^{-3}$. Hence, the 2C-death and 2C-survived lineages are likely generated by the same progenitor cell, suggesting that cells entering the 2C-like state can undergo asymmetric division.

This observation was further corroborated by cells expressing other 2C reporters, MERVL::tdTomato and Zscan4::tdTomato (Fig. 1i; Supplementary information, Fig. S1a, e, f and Video S4), by cells cultured in the 2i/LIF (two kinase inhibitors and leukemia inhibitory factor) condition that maintains a naïve ground state[18] (Supplementary information, Fig. S1f), and by chemically induced 2C-like cells[19] (Supplementary information, Fig. S1g–i and Video S5). It has been reported that naïve human pluripotent stem cells can also enter an 8-cell-like (8C-like) state, similar to the 2C-like cells in mouse ES cells.[20–22] Interestingly, we found that 8C-like human cells also undergo asymmetric division, producing one dying daughter with increasing intensity of the 8C reporter (TPRX1-GFP) and one surviving cell with reduced expression of the 8C reporter (Supplementary information, Video S6). We note that this asymmetric division is inferred from the two distinct cell fates of the daughter lineages, which are morphologically indistinguishable.

The phenotype of asymmetric progeny fates is reminiscent of budding yeast divisions, in which the aged mother cell succumbs to death after a limited number of divisions and the young daughter cell starts anew with its age reset to zero.[23] Asymmetric divisions in yeast segregate damaged cellular components from newly synthesized ones,[24,25] providing a mechanism for lineage renewal at the cost of individual aging. We hypothesize that mESCs may adopt a similar strategy for lineage renewal through asymmetric divisions in the spontaneous 2C-like state. Our hypothesis predicts the following: (1) cells entering the 2C-like state (hereafter referred to as ‘2C-entering’ cells, Fig. 1j) exhibit signs of aging marked by elevated cellular damage; (2) cells in the 2C-like state asymmetrically allocate damaged components between the two progenies, which dictate their distinct fates; (3) the 2C-survived lineage, which prevails through the asymmetric division, experiences functional rejuvenation, reflected in clonogenicity in vitro and chimeric efficiency in vivo. We tested all three predictions in this study.

2C-like cells show signs of aging

A prominent feature of aging cells is lengthening of the cell cycle.[26] Indeed, MERVL::GFP$^+$ cells took longer to progress through the cell cycle (Fig. 2a), consistent with previous reports based on fixed-cell data.[16,27–29] Cell-cycle lengthening was particularly pronounced in the 2C-entering and 2C-death subpopulations (Fig. 2b). Notably, a portion of 2C-death cells underwent prolonged cell-cycle arrest before death (Supplementary information, Fig. S2a). Using the cell-cycle phase reporter PIP-FUCCI[30] (Supplementary information, Fig. S2b), we found that this cell-cycle lengthening could be attributed to lengthening of the S and G2/M phases (Fig. 2c), consistent with the increased replication stress reported previously.[14]

This result implies that 2C-like cells may contain elevated DNA damage, another hallmark of aging.[31] Indeed, MERVL::GFP$^+$ cells show increased levels of phospho-p53, indicating an active DNA damage response (Fig. 2d). To investigate this further, we performed an unbiased transcriptomic analysis of sorted MERVL::GFP$^-$ and MERVL::GFP$^+$ cells. Single-cell RNA sequencing revealed a significant enrichment of direct p53 target genes among those upregulated in MERVL::GFP$^+$ cells ($P = 1.77 \times 10^{-6}$, hypergeometric test, Supplementary information, Fig. S2c, d). This p53 pathway activation was most pronounced in cluster 3, which expressed the highest levels of 2C markers and likely corresponded to the 2C-death subpopulation ($P = 2.46 \times 10^{-13}$, hypergeometric test, Supplementary information, Fig. S2e–g).

We next asked whether this transcriptional response corresponded to physical DNA breaks. Comet assays on sorted MERVL::GFP$^+$ cells confirmed this, showing a higher fraction of DNA in the comet tails, indicative of increased DNA breakage (Fig. 2e). Furthermore, induction of DNA damage with aphidicolin (Aph), mitomycin C (MMC), or hydroxyurea (HU) increased the proportion of MERVL$^+$ cells in a dose-dependent manner (Fig. 2f), consistent with previous reports.[13] Taken together, our results demonstrate that 2C-like cells exhibit significant DNA damage and that DNA damage itself can act as a key driver for entering the 2C-like state.

We next tested whether other types of cellular damage promote entry into the 2C-like state. Induction of oxidative stress with 2-methoxyestradiol (2-MeOE2) or induction of osmotic stress with NaCl, sucrose, or polyethylene glycol (PEG) increased the fraction of MERVL$^+$ cells (Fig. 2g), consistent with previous reports,[32] whereas endoplasmic reticulum stress did not significantly alter the percentage of MERVL$^+$ cells (Supplementary information, Fig. S2h, i). These results indicate that entry into the 2C-like state can be driven by some types of cellular damage.

DNA damage is asymmetrically segregated in the 2C-like state

Can cellular damage be asymmetrically separated in the 2C-like state? To test this possibility, we investigated the partitioning of damaged DNA between sister cells. We used time-lapse imaging of mESCs with a nuclear marker to trace their divisions and a

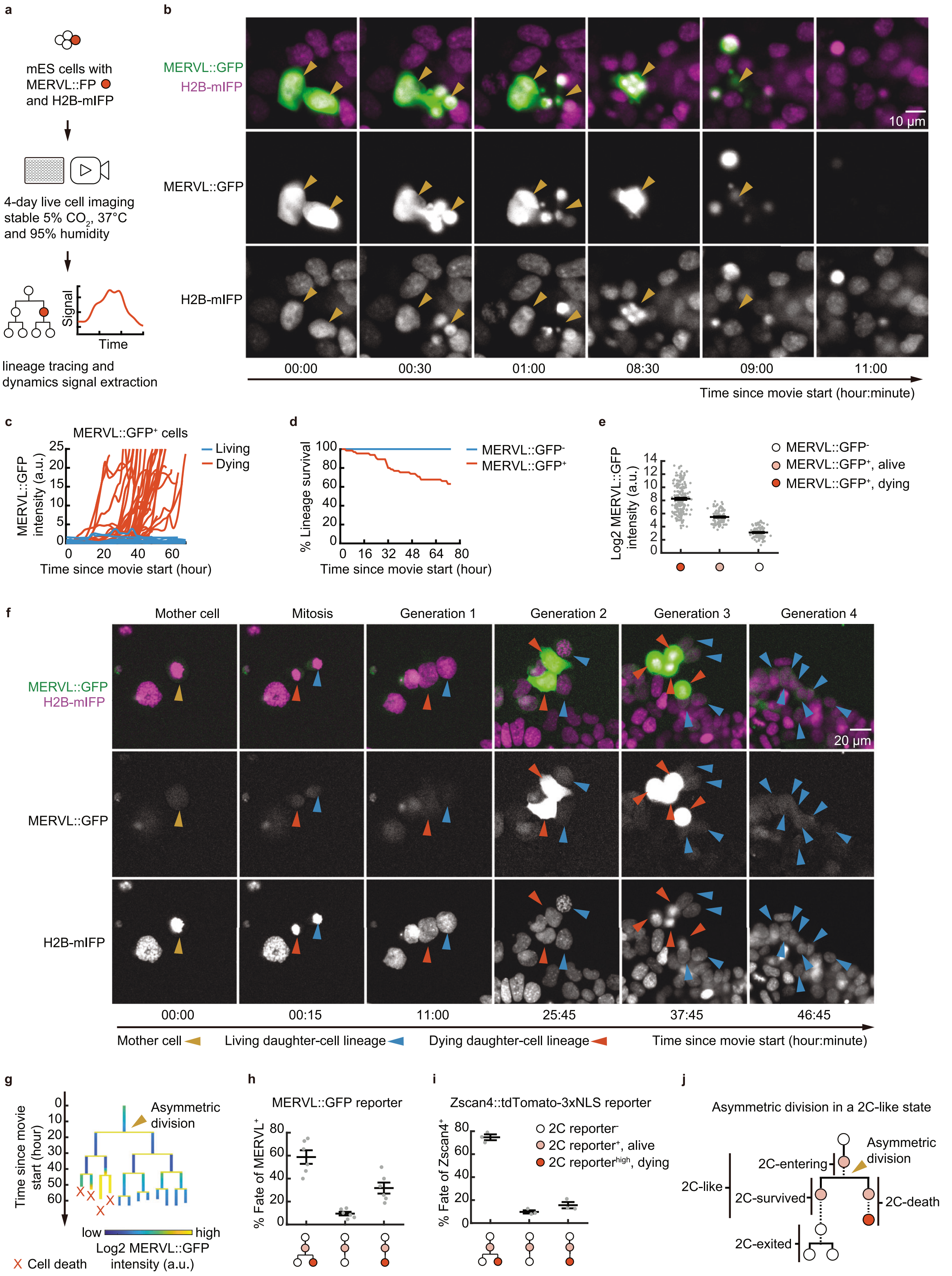

MERVL reporter to track their MERVL status. At the end of the movie, we fixed the cells and stained them with a γH2AX antibody to assess DNA damage in sister-cell pairs (Fig. 3a). Notably, asymmetric division of γH2AX was much more prevalent between MERVL$^+$ sisters divided from 2C-entering cells compared with MERVL$^-$ ones (Fig. 3b, c), indicating that damaged DNA tends to be asymmetrically segregated in the 2C-like state.

To test whether asymmetric segregation of damaged DNA correlates with the fates of 2C-like cells, we introduced a live-cell reporter of DNA damage into an mESC line with the MERVL

Fig. 1 2C reporter$^+$ cells generate asymmetric daughter-cell fates. **a** Experimental scheme of live-cell imaging experiments. mESCs were cultured in a 96-well plate with stable 5% CO_2, 37 °C, and 95% humidity. The fluorescent signal of H2B-mIFP was used to track cell lineage, and MERVL::FP was used to monitor MERVL status. FP, fluorescent protein (GFP or tdTomato). **b** Examples of MERVL::GFP$^+$ cell death, indicated by the condensation or fragmentation of H2B-mIFP signal without cell division and subsequent disappearance of the MERVL::GFP signal within 1–2 frames (15–30 min). Scale bar, 10 μm. See also Supplementary information, Fig. S1b for other examples and Supplementary information, Video S1 for the full process. **c** Dynamics of GFP intensity in MERVL::GFP$^+$ cells, grouped by their living or dying fates determined by the end of the movie ($n = 50$ in each group). **d** Lineage survival of MERVL::GFP$^+$ ($n = 65$) and MERVL::GFP$^-$ ($n = 85$) cells plotted as a Kaplan–Meier curve. For MERVL::GFP$^+$ cells, lineage was tracked from the moment of the MERVL::GFP$^-$ to MERVL::GFP$^+$ transition and classified as 'death' if all progenies died by the end of the movie or 'alive' if any progeny survived. For MERVL::GFP$^-$ cells, lineages that remained MERVL::GFP$^-$ throughout the entire movie were tracked and assessed identically. $P < 0.0001$. **e** MERVL::GFP intensity of MERVL::GFP$^-$ ($n = 95$), living ($n = 103$), and dying ($n = 190$) MERVL::GFP$^+$ cells. Each data point represents the average MERVL::GFP intensity over one cell cycle. **f** An example of a MERVL::GFP$^+$ cell producing daughter cells with distinct fates. The images, from left to right in temporal order from a timelapse movie, show the fates of all progenies from a MERVL::GFP$^+$ cell. The mother cell (yellow arrowhead), which exhibited low but above-background MERVL::GFP expression, divided into two daughter cells (columns 1–2). One daughter generated a lineage with increasing levels of MERVL::GFP (columns 3–4), and all cells died by 46 h (tracked by red arrowheads). The other daughter produced a viable lineage with diminishing MERVL::GFP levels (tracked by blue arrowheads). Scale bar, 20 μm. See Supplementary information, Video S3 for another example. **g** Lineage tree of a MERVL::GFP$^+$ cell. The cell entered a MERVL::GFP$^+$ state with low GFP intensity (0–18 h). One of its daughters showed increasing MERVL::GFP levels (starting around 42 h), and all progenies died by 60 h (marked by crosses). The other daughter produced a lineage with all progenies alive. The arrowhead indicates an asymmetric division, assigned retrospectively. The heat colors indicate the fluorescence intensity of MERVL::GFP. **h**, **i** Percentage of different daughter-cell fates of ESCs spontaneously transitioning into the 2C-like state, marked by either MERVL::GFP (**h**) or Zscan4::tdTomato (**i**). Three different fates are observed. Right: mESC (2C reporter$^-$) enters the 2C-like state, and all its progenies show increasing reporter intensity and undergo cell death (2C reporter^{high}, dying); middle: all progenies show diminishing reporter intensity and survive (2C reporter$^+$, alive); left: the cell enters a 2C-like state and generates two daughter lineages with distinct fates, one with increasing 2C reporter intensity that dies, the other with diminishing reporter intensity that survives, as exemplified in **g**. Each point represents an experiment. **j** A schematic depicting subpopulations of 2C-like cells. The subpopulations are defined in live-cell movies with the lineage dynamics. The arrowhead indicates the asymmetric division of daughter-cell fates. Error bars indicate mean ± SEM (**e**, **h**, **i**). Log-rank test (**d**). See also Supplementary information, Fig. S1 and Videos S1–S6.

reporter to monitor their temporal dynamics. The reporter consists of a fusion between the tandem Tudor domain of 53BP1 and the fluorescent protein mVenus.[33] In unperturbed naïve mESCs, endogenous 53BP1 foci, which mark double-strand breaks (DSBs), were rare compared with those of the general DNA damage marker γH2AX (Supplementary information, Fig. S3a, b), consistent with previous reports.[34–36] Our 53BP1-mVenus reporter formed foci that co-localized with both endogenous 53BP1 and γH2AX foci (Supplementary information, Fig. S3c–e). Co-localization was much more prominent with γH2AX foci than with endogenous 53BP1, indicating that 53BP1-mVenus reports on a broad range of DNA lesions rather than only DSBs. The number of foci increased after induction of DNA damage (Supplementary information, Fig. S3f), confirming the reporter's reliability.

In the live-cell imaging, both 2C-entering cells and cells one cell cycle before lighting up their 2C reporter contained more 53BP1-mVenus foci than the rest of the MERVL$^-$ cells (Fig. 3d), suggesting that DNA damage precedes entry into the 2C-like state.

We further traced the segregation of DNA damage. Importantly, 53BP1-mVenus foci were asymmetrically divided in 2C-entering cells with weak MERVL::tdTomato signals (Fig. 3e, columns 1–3) more often than in MERVL$^-$ cells (Fig. 3f). Asymmetric segregation of DNA damage occurred well before differences in 2C reporter intensity became apparent between daughter-cell lineages (Fig. 3e, columns 3 and 4; Supplementary information, Fig. S3g), suggesting that DNA damage asymmetry is likely a cause rather than a consequence of their distinct cell fates. Progenies that inherited fewer 53BP1 foci were biased towards the 2C-survived fate, whereas those that inherited more 53BP1 foci tended to adopt the 2C-death cell fate (85.19%, $P = 0.008$, permutation test) (Fig. 3e, g; Supplementary information, Video S7). This asymmetric segregation led to an overall lower number of 53BP1 foci in the 2C-survived cells than in the 2C-death cells (Fig. 3h). In addition to cells spontaneously entering the 2C-like state, DNA damage-induced 2C-like cells also showed asymmetric segregation of 53BP1 foci and an association of the 2C-death fate with a high 53BP1 foci number (Supplementary information, Fig. S3h–k). Together, these results demonstrate a strong correlation between asymmetric inheritance of DNA damage and the asymmetric cell fates observed through the 2C-like state.

How does DNA damage asymmetrically segregate into the two sisters? We hypothesized that the asymmetric segregation relies on the perception of DNA damage. By treating cells with inhibitors of ATM, ATR, CHEK, or PARP, we observed that silencing the DNA damage response significantly reduced the fraction of 2C-like cells that generated asymmetric daughter lineage fates (Fig. 3i). Among the 2C-like cells that did give rise to asymmetric fates, the division of 53BP1 foci was less asymmetric in cells treated with ATM, ATR, CHEK, or PARP inhibitors compared with control cells (Fig. 3j). This result was further confirmed by shRNA-mediated knockdown of ATM, ATR, CHEK, or PARP (Fig. 3k, l; Supplementary information, Fig. S3l, m). Together, these data suggest that the DNA damage response is essential for asymmetric segregation of DNA damage, which in turn mediates the asymmetric fates of daughter lineages.

We further hypothesized that the cell-division machinery plays a role in the asymmetric segregation of damaged DNA. In budding yeast, the inherent asymmetry of the spindle pole body (SPB, centrosome equivalent in yeast) is directly associated with the differential fates of daughter cells: the old SPB migrates to the bud, whereas the new one remains in the larger mother cell.[37] This age difference lays the foundation for the structural and functional asymmetry of the two SPBs. To test whether this mechanism is conserved in the asymmetric division of 2C-like cells, we labeled the old centrosome in mESCs using the appendage marker EGFP-Ninein[38] and followed centrosomes and cell fates using live-cell imaging. Indeed, centrosome segregation was non-random between the two 2C fates: the old centrosome was strongly biased towards the 2C-death lineage ($P = 0.024$, Fig. 3m), suggesting that 2C-like cells may exploit a mechanism of asymmetric division similar to that found in yeast.

Functional heterogeneity of 2C-like cells

To test the prediction of functional rejuvenation, we assessed the functional status of mESCs going through different stages of the 2C-like cycle. First, we examined whether the 2C-death and 2C-survived fates could be distinguished by the fluorescence intensity of 2C reporters in a snapshot. We sorted cells with high 2C reporter intensity (reporter-high, top 0.5% for MERVL and top 1% for Zscan4) and lower, but above-background, 2C reporter intensity (reporter-low, 98.5%–99.5% for MERVL or 98%–99% for

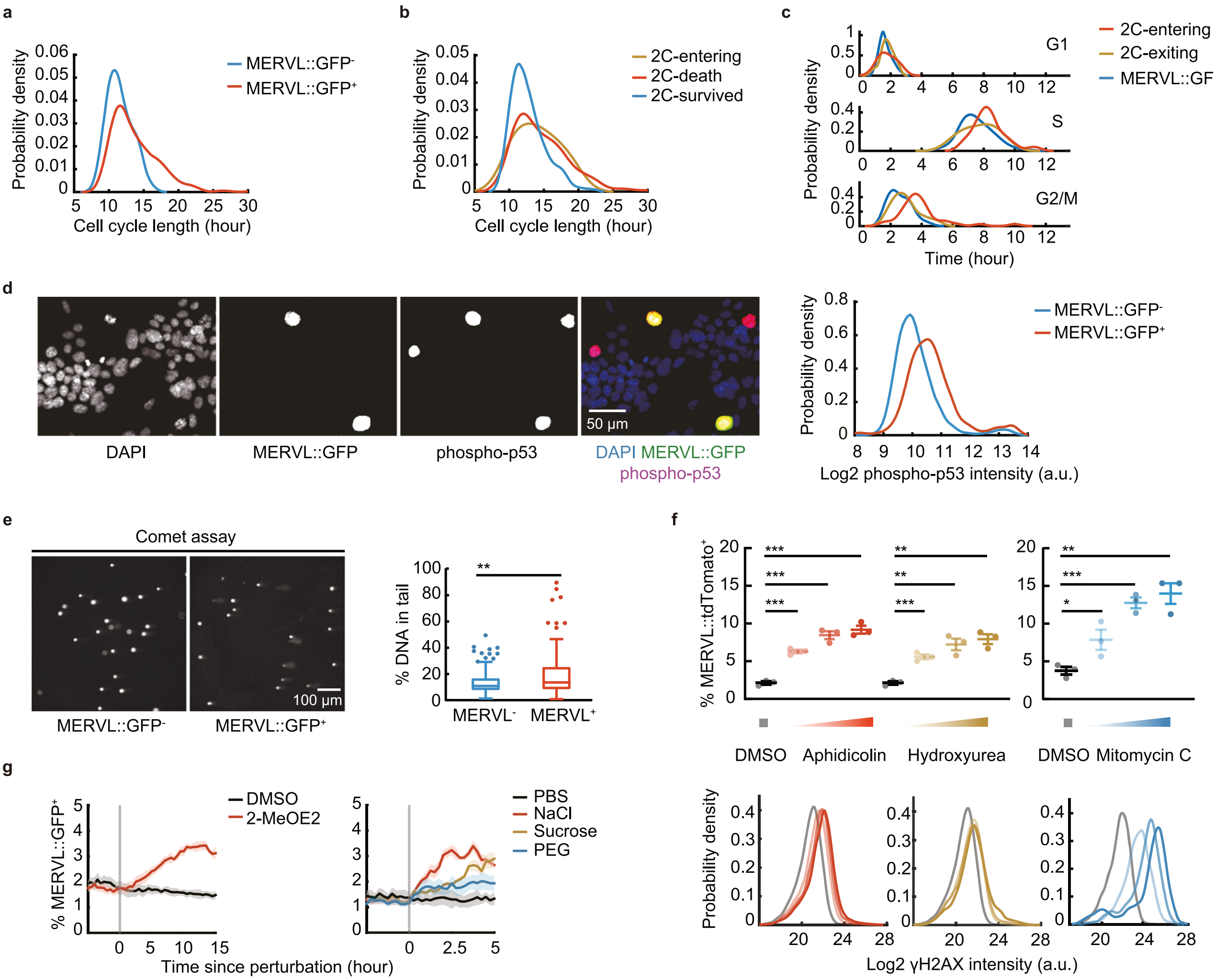

Fig. 2 2C-like cells show signs of aging. a A density plot shows the probability distribution of cell-cycle length of MERVL::GFP-positive ($n = 269$) and negative ($n = 100$) cells, measured as the time between two consecutive mitoses marked by the segregation of H2B-mIFP in live-cell imaging experiments. The *y*-axis (probability density) represents the likelihood of a cell having a particular cycle length. The area under the entire curve sums to 1, meaning that the curve depicts the full distribution of probabilities. $P < 0.0001$. **b** Cell-cycle length of 2C-survived ($n = 150$), 2C-entering ($n = 53$, $P < 0.01$), and 2C-death ($n = 125$, $P < 0.0001$) cells among the MERVL::GFP$^+$ lineages that undergo asymmetric division. **c** Length of cell-cycle phases in the 2C-entering (G1: $n = 33$; G2: $n = 37$; S: $n = 23$), 2C-exiting (G1: $n = 33$; G2: $n = 34$; S: $n = 26$), and MERVL::GFP$^-$ (G1: $n = 106$; G2: $n = 92$; S: $n = 80$) cells, determined by PIP-FUCCI-mCherry and H2B-mIFP reporters. See more details in Supplementary information, Fig. S2b. The 2C-entering cells exhibit significant lengthening of the S phase ($P < 0.01$) and G2/M phase ($P < 0.0001$) compared with MERVL::GFP$^-$ cells. **d** Phospho-p53 staining in MERVL::GFP$^+$ and MERVL::GFP$^-$ cells. Left, representative images; right, probability density distribution of phospho-p53 intensity in single cells (610 MERVL$^+$ cells and 60,342 MERVL$^-$ cells). $P < 0.0001$. Scale bar, 50 µm. **e** Comet assay of sorted MERVL::GFP$^+$ and MERVL::GFP$^-$ cells. Left, representative images; right, quantification of the tail DNA fraction ($n = 128$ for each group). Scale bar, 100 µm. **f** Top: the percentage of MERVL::tdTomato$^+$ cells in DNA damage conditions, $n = 3$; bottom, the probability density distributions of mean γH2AX intensity in DNA damage conditions ($n > 1000$ for each curve). **g** The percentage of MERVL::GFP$^+$ cells upon application of oxidative (left) and osmotic stress (right), $n = 4$ for each group. The dotted lines indicate the start of dosing. Error bars indicate mean ± SEM (**f**). Data are presented as 95% confidence intervals (**g**). Mann–Whitney U test (**a–c, e**); Kolmogorov–Smirnov test (**d**); two-tailed unpaired Student's *t*-test (**f**). See also Supplementary information, Fig. S2.

Zscan4) into separate wells and followed the fates of these cells using live-cell imaging (Fig. 4a, b). More than 70% of the 2C reporter-high cells died within 48 h, consistent with the 2C-death fate (Fig. 4c). The rare surviving reporter-high cells had fewer 53BP1 foci than the majority that died (Supplementary information, Fig. S4a). By contrast, 2C reporter-low cells had a comparable probability of dying, returning to a reporter-negative state, or undergoing asymmetric division (Fig. 4d). Therefore, whereas 2C-death cells can be readily identified in a snapshot by their high reporter intensity, cells with low reporter intensity comprise a mixture of cells entering the 2C-like state that will undergo asymmetric division, 2C-death cells that are increasing their 2C reporter intensity, and 2C-survived cells (Fig. 4e).

Functionally, reporter-high cells generate substantially fewer alkaline phosphatase-positive (AP-positive) clones than unsorted and reporter-low cells in clone assays (Fig. 4a, f, g). To further test their ability to contribute to embryonic development, we injected them into 8C embryos and tested chimera formation at the blastocyst stage (Fig. 4a). Both reporter-high and reporter-low cells were able to contribute to the trophectoderm (TE) and inner cell mass (ICM), in contrast to reporter-negative cells, which contributed exclusively to the ICM (Fig. 4h, i; Supplementary information, Fig. S4b). However, compared with reporter-low cells, a significantly smaller fraction of reporter-high cells contributed to chimera formation (Fig. 4j; Supplementary information, Fig. S4c). These results suggest that

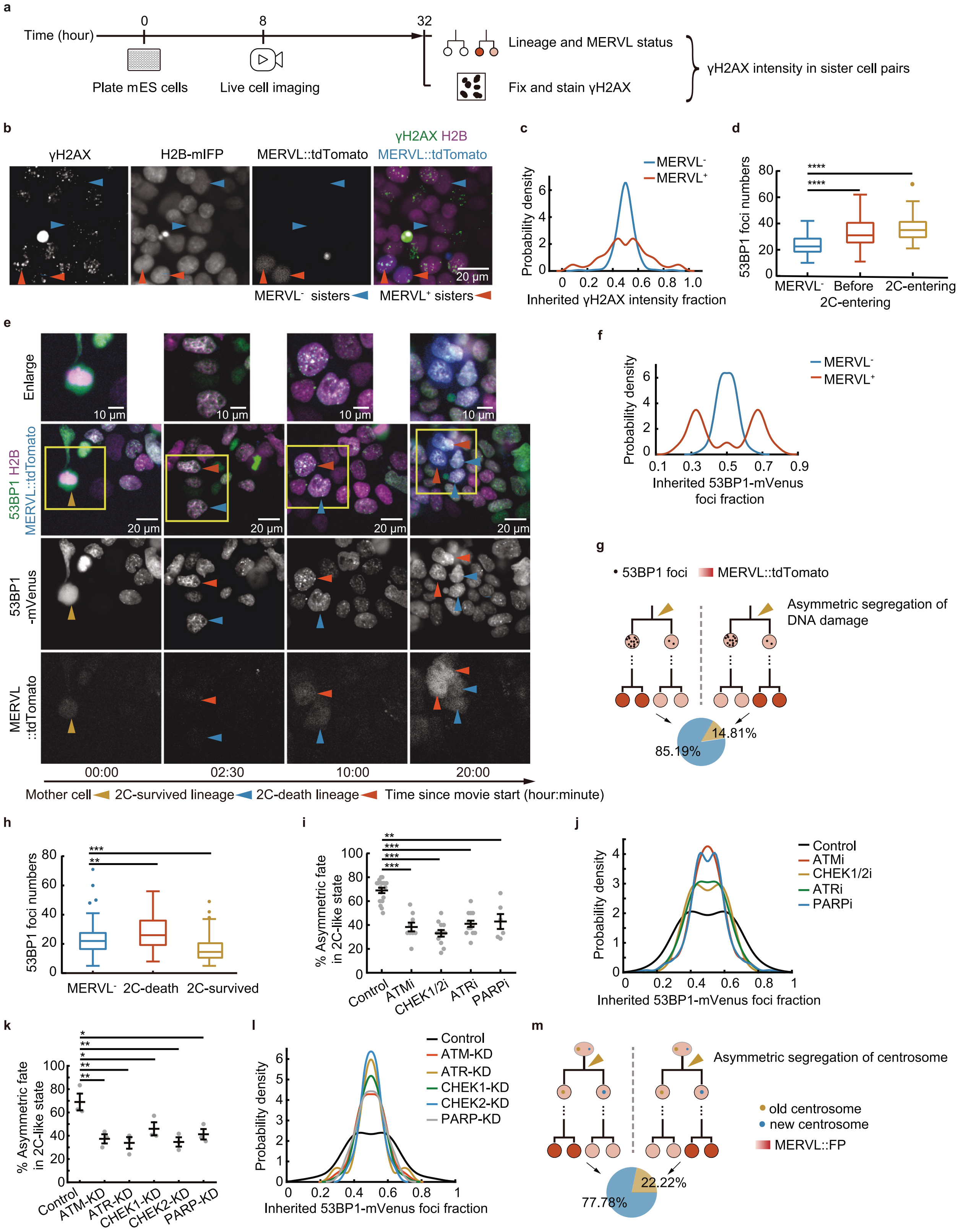

cells with high 2C reporter intensity primarily adopt a dying fate and are less capable of contributing to embryonic development, supporting our model that they represent the damage-enriched lineage.

Rejuvenation of 2C-exited cells

Next, we investigated the functional and molecular status of cells exiting from the 2C-like stage. Since cells with low 2C reporter intensity are a mixture of 2C-survived, 2C-entering, and early-stage

Fig. 3 Asymmetric division of DNA damage in 2C reporter$^+$ cells. a Experimental design of **b** and **c**. Live-cell imaging was performed to obtain cell lineage and MERVL status, followed by fixation and anti-γH2AX staining at the endpoint to compare γH2AX intensity between sister cells. **b** Representative γH2AX staining in MERVL::tdTomato$^+$ (red arrowheads) and MERVL::tdTomato$^-$ (blue arrowheads) sisters. Scale bar, 20 μm. **c** Probability density distribution of the inherited γH2AX fraction between 2C-entering MERVL::tdTomato$^+$ or MERVL::tdTomato$^-$ sisters: γH2AX intensity of each sister divided by the sum of the pair ($n = 97$ pairs for each group). $P < 0.0001$. **d** Numbers of 53BP1-mVenus foci in 2C-entering ($n = 56$), before 2C-entering (one cell cycle before the 2C reporter lights up, $n = 53$) and MERVL$^-$ cells ($n = 56$). **e** A representative division of 53BP1-mVenus foci in the MERVL$^+$ cell lineage. The daughter cell that inherited more 53BP1 foci (columns 1–3) became the 2C-death lineage with higher MERVL::tdTomato intensity (columns 3–4). Yellow arrowhead, MERVL$^+$ mother cell; red arrowheads, 2C-death lineage; blue arrowheads, 2C-survived lineage. Scale bars, 20 μm. Top row, enlarged images with 10-μm scale bars. See Supplementary information, Video S7 for the full progress. **f** Probability density distribution of the inherited 53BP1-mVenus foci fraction: number of foci of each sister divided by the sum of the pair ($n = 54$ pairs for each condition). $P < 0.0001$. **g** Schematic depicting the two correlation modes between asymmetric segregation of 53BP1 foci number and asymmetric division of MERVL$^+$ cells. Left, cells inheriting more 53BP1 foci adopt the 2C-death fate; right, cells inheriting more 53BP1 foci adopt the 2C-survived fate. The proportion of the two is shown in the pie chart ($n = 54$, $P = 0.008$). **h** Numbers of 53BP1 foci in MERVL$^-$ ($n = 108$), 2C-death ($n = 54$), and 2C-survived daughter cells ($n = 54$). **i** Percentage of asymmetric division in 2C-like cells when the DNA damage response is inhibited by ATM, CHEK, ATR, or PARP inhibitors (ATMi, $n = 9$; CHEKi, $n = 12$; ATRi, $n = 13$; PARPi, $n = 6$; control, $n = 18$). **j** The probability density distribution of inherited 53BP1-mVenus foci fraction in daughter cells upon inhibition of the DNA damage response: number of foci of each sister divided by the sum of the pair. Control ($n = 118$ pairs), ATMi ($n = 31$ pairs, $P < 0.01$), CHEK1/2i ($n = 31$ pairs, $P < 0.05$), ATRi ($n = 31$ pairs, $P < 0.05$), PARPi ($n = 84$ pairs, $P < 0.001$). **k** Percentage of asymmetric divisions in 2C-like cells when ATM, CHEK, ATR, or PARP was knocked down ($n = 3$ in each group). **l** The density distribution of inherited 53BP1-mVenus foci fraction in daughter cells upon knockdown of ATM, CHEK, ATR, or PARP: number of foci of each sister divided by the sum of the pair. Control ($n = 28$ pairs), ATM-KD ($n = 25$ pairs, $P < 0.05$), CHEK1-KD ($n = 19$ pairs, $P < 0.05$), CHEK2-KD ($n = 24$ pairs, $P < 0.01$), ATR-KD ($n = 15$ pairs, $P < 0.05$), PARP-KD ($n = 16$ pairs, $P < 0.05$), KD, knockdown. **m** Segregation of the ninein marker reveals that new and old centrosomes are correlated with different daughter-cell lineage fates in MERVL::tdTomato$^+$ cells ($n = 36$ pairs, $P = 0.024$). Error bars indicate mean ± SEM (**i**, **k**). Mann–Whitney U test (**d**, **h**, **i**, **k**); Kolmogorov–Smirnov test (**c**, **f**, **j**, **l**); permutation test (**g**, **m**). See also Supplementary information, Fig. S3 and Video S7.

2C-death cells, they cannot be separated on the basis of 2C reporter intensity alone (Fig. 4e). To sort 2C-survived cells and their recent descendants, we used a tandem fluorescent protein timer that encodes the temporal dynamics of transcription into the ratio of two fluorescence signals in a snapshot.[39,40] Specifically, this sensor consists of the fast-maturing and fast-degrading fluorescent protein (FP) sfGFP-PEST and the slow-maturing and slow-degrading FP DsRed2, both expressed under the control of the MERVL promoter (Fig. 5a). Upon cell entry into the 2C-like state, the MERVL promoter switches on, simultaneously producing both FPs, but sfGFP-PEST matures before DsRed2. After deactivation of the MERVL promoter, DsRed2 persists within cells for much longer than sfGFP-PEST (Fig. 5b). Therefore, the fluorescence ratio between the two FPs reflects the time relative to the on/off status of the MERVL promoter (Fig. 5c; Supplementary information, Fig. S5a).

Using this reporter, we sorted cells that had recently exited from the 2C-survived branch (DsRed2$^+$sfGFP-PEST$^-$, Fig. 5c). Compared with the subpopulation that had not recently passed through the 2C-like state (DsRed2$^-$sfGFP-PEST$^-$), sorted 2C-exited cells showed better dome-shaped colony morphology and fewer signs of DNA damage (Fig. 5d–f). They also showed more robust staining of pluripotency markers such as AP, Nanog, and Oct4 (Fig. 5g, h; Supplementary information, Fig. S5b, c). At the transcriptome level, pluripotent marker genes were overall upregulated in DsRed2$^+$ cells compared with DsRed2$^-$ cells (Fig. 5i, j). DsRed2$^+$ cells also generated more AP$^+$ clones in clone assays than DsRed2$^-$ cells and the unsorted mESC subpopulations (Fig. 5k; Supplementary information, Fig. S5d). However, overexpression of Nanog did not rescue the reduced clone-forming capacity of DsRed2$^-$ cells (Fig. 5k), suggesting that reduced Nanog expression is likely a consequence rather than a cause of impaired pluripotency in DsRed2$^-$ cells.

To determine the longevity of the enhanced pluripotency in DsRed2$^+$ cells, we sorted DsRed2$^+$ and DsRed2$^-$ cells and remeasured the distribution of Nanog intensity daily. Interestingly, the two subpopulations took less than 5 days to re-establish the steady state of Nanog expression (Fig. 5l), suggesting that the gained pluripotency has an average lifetime of fewer than 10 generations.

We next tested the pluripotency of 2C-exited cells in vivo in chimera assays. When 2C-exited cells were injected into mouse blastocysts, 73.3% of the embryos were chimeras with contributions from the donor cells (BFP$^+$), a much higher efficiency than that obtained using the DsRed2$^-$ cells (12.8%) (Fig. 5m–o; Supplementary information; Fig. S5e–h). Collectively, these results indicate that cells that have survived from the asymmetric divisions and recently exited the 2C-like state show enhanced pluripotency, akin to a functionally rejuvenated state.

It remains controversial whether passing through the 2C-like state is essential for maintenance of long-term pluripotency of mESC culture.[9,10] We tested this by knocking down *Zscan4* (Supplementary information, Fig. S5i, j) or knocking out DUX (Supplementary information, Fig. S5k) to suppress entry into the 2C-like state. Both perturbations greatly reduced MERVL$^+$ cells[13] (Supplementary information, Fig. S5l, m) and resulted in attenuated pluripotency of mESCs, as shown in clone assays (Fig. 5p, q). Together, our data suggest that entry into the 2C-like state is indeed an important mechanism for rejuvenation of the ESC lineage despite aging of individual cells (Fig. 5r).

DISCUSSION

Our data support a model in which seemingly symmetrically dividing mESCs leverage asymmetric divisions during a sporadic 2C-like state to extend their lineages. By selectively concentrating damage into one daughter cell, this division generates two progenies that differ in functional age: a compromised one enriched in damage and a rejuvenated one with enhanced pluripotency. Quantitatively, the rejuvenation effect persists for 8–10 generations (Fig. 5l). From a population dynamics perspective, this translates into a requirement that only 0.1%–0.4% of cells undergo a rejuvenating event per generation (i.e., 1 cell in every 256–1024). This calculated requirement falls well within the observed size of the 2C-like cell population, demonstrating that sporadic entry into this state is quantitatively sufficient to power long-term self-renewal of the entire ESC culture.

Consistent with this model, our data demonstrate that 2C-like cells are functionally heterogeneous, exhibiting significant variability in their chimeric capability. This finding challenges the conventional view of 2C-like cells as a single population and reconciles seemingly contradictory findings in the field: although 2C-like cells exhibit elevated DNA damage and cell death suggesting a compromised state, blocking their formation triggers

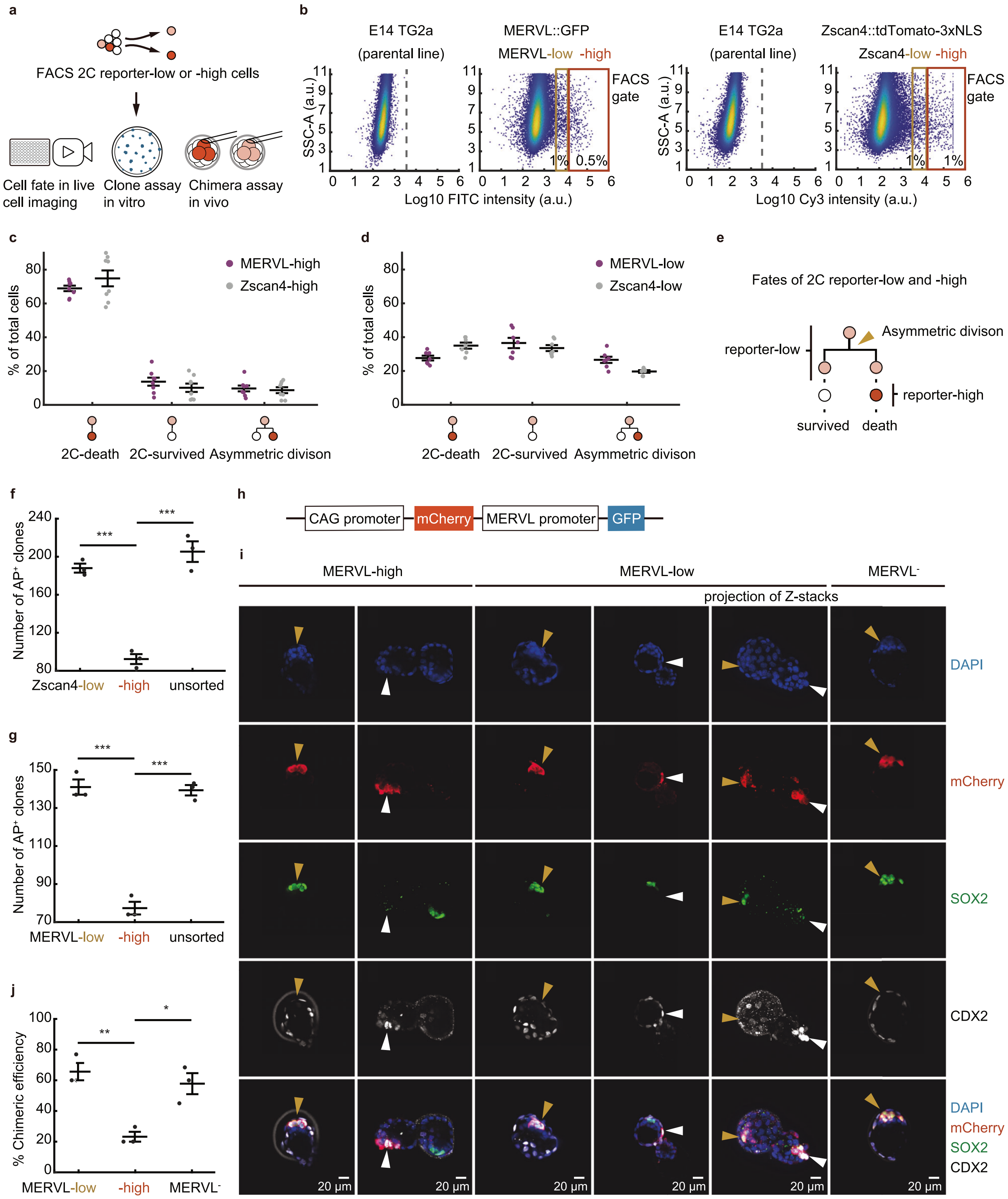

a culture crisis in mESCs, indicating that they have an essential role in self-renewal. Our model unifies these observations by proposing that the 2C-like state produces divergent lineages: one destined for elimination that accounts for the observed damage, and another that ensures lineage renewal.

This model represents a solution for managing damage in immortal cell lineages. Although asymmetric division is well established in morphologically asymmetric systems like budding yeast, it has not been clear whether other morphologically symmetrically dividing cells have the potential to generate daughter cells with distinct ages. Observation of asymmetric divisions in simple organisms such as *E. coli* implies that the prevalence of such divisions and their association with cellular aging might be more widespread than previously envisioned.[41] Although the 2C-like state may be unique to mESCs, we hypothesize that the downstream machinery that mediates

Fig. 4 Functional heterogeneity of 2C reporter$^+$ cells. a Experimental design of **b**–**j**. 2C reporter-high or reporter-low subpopulations were sorted by fluorescence-activated cell sorting (FACS) for live-cell imaging, clone assays, and chimera assays. **b** Sorting gates for 2C reporter-low and reporter-high subpopulations in MERVL::GFP (left) and Zscan4::tdTomato-3×NLS (right) cell lines. **c, d** Percentage of 2C-death, 2C-survived, and asymmetric division in 2C reporter-high (**c**) or reporter-low (**d**) cells within 48 h after FACS. **e** A schematic depicting the fates of 2C reporter-low and reporter-high cells. The arrowhead indicates the asymmetric division. **f, g** Clone assays of 2C reporter-low, 2C reporter-high, and unsorted cells (**f**, Zscan4 reporter; **g**, MERVL reporter). The numbers of AP$^+$ colonies were quantified. **h** The construct used in the chimera experiments in **i** and **j**. mCherry served as a tracer of donor cells. **i** Immunofluorescent staining of chimeric blastocysts incorporating donor cells (labeled by mCherry) from sorted MERVL-low, MERVL-high, and MERVL$^-$ cells. SOX2, ICM marker; CDX2, TE marker. Yellow arrowheads indicate mCherry$^+$SOX2$^+$ cells; white arrowheads indicate mCherry$^+$CDX2$^+$ cells. Scale bar, 20 μm. Images are from a single *Z* position with the exception of column 5, which is the maximum intensity projection of *Z* stacks. **j** Chimeric efficiency of MERVL-low, MERVL-high, and MERVL$^-$ cells. Each dot represents chimeric efficiency (mCherry$^+$/total embryo number) in an independent experiment. Error bars indicate mean ± SEM (**c**, **d**, **f**, **g**, **j**). Two-tailed unpaired Student's *t*-test (**f**, **g**, **j**). See also Supplementary information, Fig. S4.

asymmetric damage segregation may be conserved across various immortal lineages. From bacterial aging to germline-soma segregation, and even the queen-worker differentiation in eusocial insects like bees, the asymmetric division in mESCs exemplifies a broader principle: progeny asymmetries at different levels can generate diversity for selection within a population, enabling lineage renewal at the expense of a disposable subset. As the first such example in mammalian cells, mESCs offer a unique model for studying cellular aging and rejuvenation.

Historically, telomeres have been recognized as the primary determinant of replicative lifespan. However, the discovery of telomerase and alternative lengthening mechanisms suggests that telomeres impose a signaling limit rather than an absolute barrier.[42,43] Instead, spontaneous cellular damage is an inevitable source of cellular aging. Our data suggest that asymmetric divisions serve as a critical mechanism to partition this damage, and the capacity for such divisions may thus act as a key control knob for lineage renewal, with practical consequences for disease and regeneration. For example, by targeting stem cell exhaustion, a hallmark of organismal aging and a major hurdle in regenerative medicine, our findings highlight a potential avenue by inducing asymmetric division in stem cells. Conversely, in cancer, it may be possible to block undesired lineage rejuvenation by manipulating asymmetric divisions. Intriguingly, the 2C markers DUX4 and ZSCAN4 are expressed in many human cancers,[44] often in a small subpopulation.[45] ZSCAN knockdown in human head and neck squamous cell carcinoma reduced its amplification and tumor formation capability.[46] Whether asymmetric division occurs in this context is open to further study. This also raises a broader question: do mammalian cells leverage asymmetric division to rejuvenate their lineages in vivo? A prerequisite for answering this question is the identification of molecular markers to identify candidate cells. The 2C-like subpopulation of mESCs presents a valuable model with which to dissect the machinery that contributes to differential partitioning of damaged components and to identify conserved molecular markers that can serve as a 'footprint' for rejuvenation.

MATERIALS AND METHODS

Manufacturer names, catalog numbers, and Research Resource Identifiers (RRIDs) are provided in Supplementary information, Table S1.

Mice

The mice were fed a normal diet and housed at 20–25 °C with 30%–70% humidity and a 12-h light-dark cycle. All procedures related to animals were performed according to the ethical guidelines of the Guangzhou National Laboratory and approved by the Guangzhou National Laboratory Animal Care and Use Committee.

Cell culture

Unless otherwise specified, mESCs were maintained in serum/LIF medium composed of high glucose DMEM supplemented with 15% fetal bovine serum (FBS), 1 mM sodium pyruvate, 0.1 mM non-essential amino acids (NEAA), 2 mM GlutaMAX, 0.1 mM β-mercaptoethanol, and 25 ng/mL mouse leukemia inhibitory factor (mLIF). The serum-free 2i/LIF medium contained a 1:1 mix of DMEM/F12 and Neurobasal with 0.1 mM NEAA, 2 mM GlutaMAX, 0.5× N2 supplement, 0.5× B27 supplement, 25 ng/mL mLIF, 3 μM CHIR-99021, 1 μM PD032590, and 0.1 mM β-mercaptoethanol. The medium was changed daily. Cells were passaged with 0.05% trypsin-EDTA every 2–3 days. Culture plates were coated with 0.1% gelatin for at least 20 min at 37 °C. For live-cell imaging, phenol red-free DMEM or DMEM/F12 was used to reduce background fluorescence. For C57 ESC lines, 2i was added to the serum/LIF medium.

To convert mESCs into chemically induced totipotent stem cells (ciTotiSCs), ESCs were cultured in ciTotiSC induction medium.[19] This medium consisted of KnockOut DMEM basal medium supplemented with 5% KSR, 1× Chemically Defined Lipid Concentrate, 1% N2 supplement, 1× L-GlutaMAX, 1× penicillin–streptomycin, 1× NEAA, 1× sodium pyruvate, 55 μM β-mercaptoethanol, and 1000 U/mL mLIF. In addition, the medium was supplemented with 50 ng/mL sodium L-ascorbyl-2-phosphate, 2.5 μM 1-azakenpaullone, 0.5 μM WS6, and 0.2 μM TTNPB. Cells were passaged at a ratio of 1:5 using 0.05% trypsin-EDTA and subsequently replated onto inactivated mouse embryonic fibroblast (MEF) feeder layers.

The human TPRX1-GFP reporter iPSC (induced pluripotent stem cell) line was a kind gift from Dr. Miguel A. Esteban. To generate human naïve iPSCs that contained 8C-like cells, the primed TPRX1-GFP reporter iPSCs were washed once with DPBS, dissociated into single cells using TrypLE, and seeded at a density of 20,000 cells per well in a six-well plate pre-coated with feeder and cultured in mTeSR1 medium supplemented with 10 μM Y-27632. After 24 h, the medium was replaced with 4C-like medium.[21] The 4C-like medium was composed of a 1:1 mix of Neurobasal and Advanced DMEM/F12, 0.5× N2, 1× B27, 1× sodium pyruvate, 1× NEAA, 1× GlutaMAX, 1× penicillin–streptomycin, 10 nM DZNep, 5 nM TSA, 1 μM PD0325901, 5 μM IWR-1, 20 ng/mL human LIF, 20 ng/mL activin A, 50 μg/mL L-ascorbic acid, and 0.2% (v/v) Matrigel. These cells were maintained on a feeder layer in 4C-like medium in a humidified incubator at 37 °C with 5% CO_2 and 5% O_2. At passage 5, the cells were trypsinized into a single-cell suspension, stained with 1× SPY650-DNA probe to label the nuclei, and seeded onto a 96-well glass plate containing feeders for live-cell imaging.

Unless otherwise specified, all cells were cultured in a humidified incubator at 37 °C with 5% CO_2. All cells were tested routinely to ensure mycoplasma-free culture conditions.

Construction of stable cell lines

To establish MERVL::GFP, Zscan4::tdTomato-3×NLS, and MERVL::sfGFP-PEST-P2A-DsRed2 reporter cell lines and the CAG::GFP control cell line, we cloned the MERVL, *Zscan4*, or *CAG* promoter into PiggyBac plasmids, positioning it upstream of the respective fluorescent protein coding sequences. The MERVL promoter has been reported previously.[9] The *Zscan4* promoter, kindly shared by Dr. Yangming Wang, covers the region between the *Zscan4d* start codon and the 2570-bp upstream site from the start codon. The PEST sequence is used for rapid degradation of sfGFP.[47] The plasmid used to generate the MERVL::tdTomato cell line was kindly shared by Dr. Samuel Pfaff on Addgene (40281).[9] The *CAG* promoter-driven mCherry was added to the MERVL::GFP construct for lineage tracing in the chimera assays in Fig. 4. The resulting constructs were transfected into E14 TG2a ESCs using Lipo3000. We first enriched transfected cells by selection with the antibiotic resistance carried on the plasmids. We then isolated single cells by FACS, regardless of their fluorescent reporter expression. Clones with moderate expression levels and correct expression patterns of the reporter were used in imaging experiments. The CAG::GFP control cell

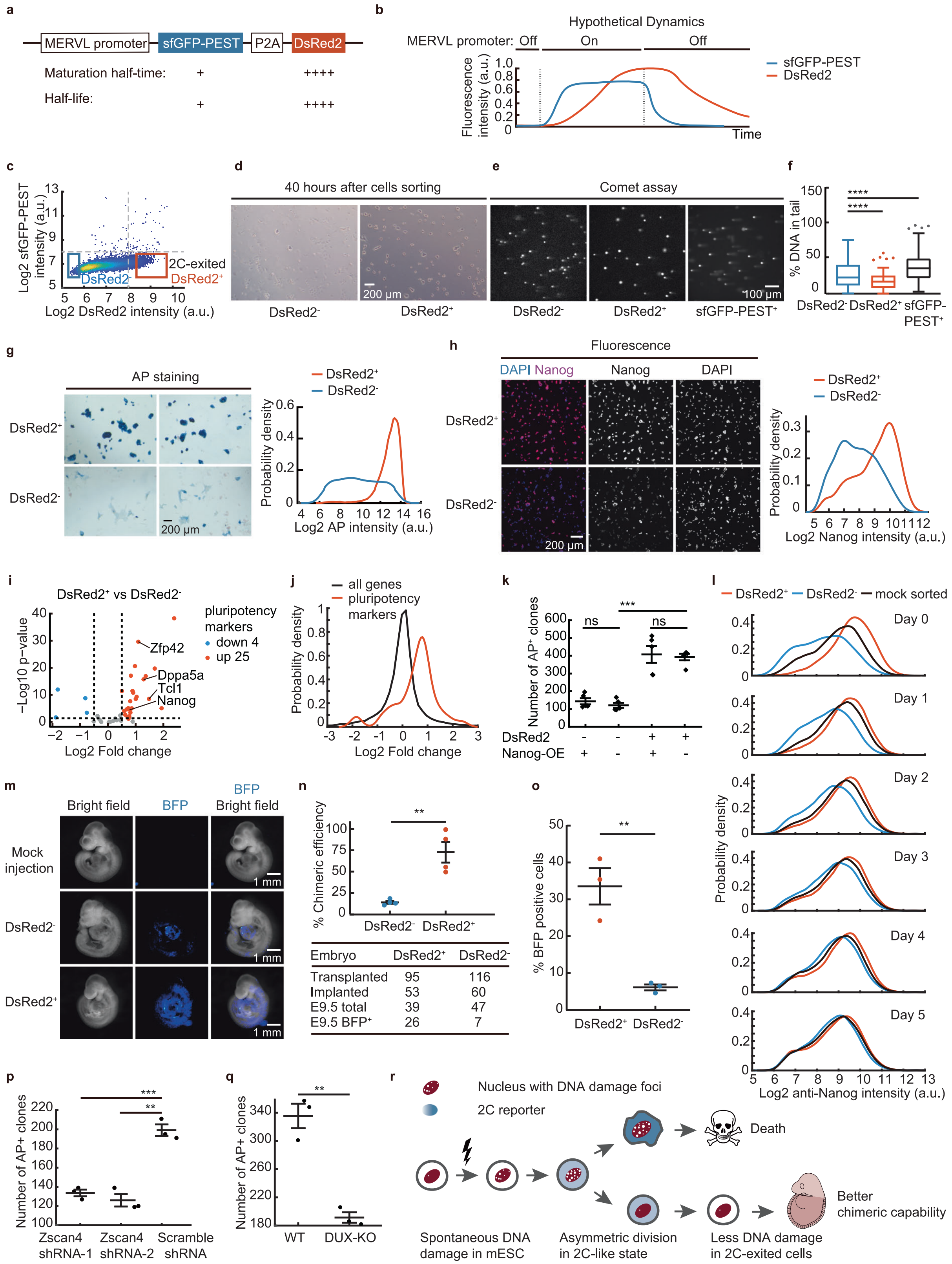

Embryo	DsRed2+	DsRed2-
Transplanted	95	116
Implanted	53	60
E9.5 total	39	47
E9.5 BFP+	26	7

line was generated as a stable, polyclonal population following drug selection.

For chimera assays of the DsRed2$^{+/-}$ cells in Fig. 5, the PiggyBac plasmid containing the fluorescent protein BFP under the control of the EF1α promoter was transfected into the MERVL::sfGFP-PEST-P2A-DsRed2 reporter cell line to label donor cells.

For cell tracking, H2B-mIFP[17] was introduced into 2C-reporter cell lines using lentiviral transduction. Lentivirus was also used to transduce PIP-FUCCI-mCherry[30] into MERVL::GFP cells to monitor cell-cycle phases and 53BP1-mVenus into MERVL::tdTomato cells to monitor DNA damage. The 53BP1-mVenus fragment consists of the tandem Tudor domain of 53BP1 (protein sequence from 1218 to 1715)[48] fused to the mVenus fluorescent protein.

Fig. 5 mESCs that recently exited the 2C-like state show improved pluripotency. **a** Design of the fluorescent timer reporter. **b** Schematics showing the hypothetical temporal dynamics of the two fluorescent proteins when cells pass through the 2C-like state. **c** Density scatter plot of sfGFP-PEST vs DsRed2 intensity in single cells. The red and blue boxes indicate the sorting gate for the DsRed2$^+$sfGFP-PEST$^-$ and DsRed2$^-$sfGFP-PEST$^-$ subpopulations (4% of total for each), respectively. The red-boxed, DsRed2$^+$sfGFP-PEST$^-$ subpopulation contains the cells that have just exited the 2C-like state, and the blue-boxed, DsRed2$^-$sfGFP-PEST$^-$ subpopulation contains the cells that have not recently been through the 2C-like state. See the correlation between this reporter and endogenous anti-MERVL-Gag staining in Supplementary information, Fig. S5a. **d** Clone morphology of the sorted subpopulations in **c** cultured under standard conditions for 40 h after FACS. Scale bar, 200 µm. **e**, **f** Comet assay of the sorted subpopulations in **c**; representative images (**e**) and quantification of the tail DNA fraction (**f**). $n = 159$ for each group. Scale bar, 100 µm. **g** AP staining of the sorted subpopulations in **c**. Left, representative images in brightfield; right, probability density distribution of AP intensity in the Cy5 fluorescent channel. $n > 4000$ for each group. Scale bar, 200 µm. **h** Nanog antibody staining of the sorted subpopulations in **c**. Left, representative images; right, quantification. $n > 6000$ for each group. Scale bar, 200 µm. **i** Volcano plot of pluripotency markers in the subpopulations sorted in **c**. **j** Probability density distribution of the fold change of pluripotency marker genes and all genes. **k** Clone assays of the sorted subpopulations in **c** with cells expressing tetracycline-inducible Nanog. The numbers of AP$^+$ colonies were quantified. **l** Probability density distribution of Nanog antibody staining 5 days after sorting and culturing the subpopulations in **c**. $n > 10{,}000$ for each group. **m** Representative images of non-chimeric and chimeric embryos incorporating donor cells (labeled by BFP) from the sorted subpopulations in **c**. Scale bar, 1 mm. **n** Chimeric efficiency of the two sorted subpopulations in **c**. **o** Percentage of BFP-positive cells in chimeric embryos, quantified by FACS. **p** Clone assays of cells expressing *Zscan4* shRNA or a scramble control. Numbers of AP$^+$ colonies were quantified. **q** Clone assays of DUX knockout (DUX-KO) and wild-type (WT) C57 mESC lines. Numbers of AP$^+$ colonies were quantified. **r** A model of asymmetric division in a 2C-like state rejuvenating the mESC lineage. During routine proliferation, mESCs accumulate DNA damage over time. Upon entering a 2C-like state, they undergo asymmetric division that segregates damage asymmetrically. One daughter lineage becomes damage-enriched and undergoes cell death, whereas the other is functionally rejuvenated, with a reduced damage burden. Error bars indicate mean ± SEM (**k**, **n**–**q**). Two-tailed unpaired Student's *t*-test (**k**, **n**–**q**); Mann–Whitney U test (**f**). See also Supplementary information, Fig. S5.

To overexpress Nanog, Nanog-T2A-EGFP was cloned into PiggyBac plasmids with the Tet-on inducible expression system and transfected into MERVL::sfGFP-PEST-P2A-DsRed2 cells. Transfected cells were selected in 200 µg/mL hygromycin. Nanog expression was induced with 1 µg/mL doxycycline.

The shRNA sequence against *Zscan4* has been reported previously.[6,49] The shRNA was introduced into E14 TG2a ESCs using lentiviral transduction and expressed under the control of the U6 promoter. Transduced cells were selected in 1 µg/mL puromycin for 5 days.

The DUX-KO C57 ESCs were derived from a single clone isolated from a DUX$^{-/-}$ blastocyst and genotyped by PCR.

The EGFP-Ninein plasmid was kindly shared by Dr. Michel Bornens on Addgene (73519).[50] To track old and new centrosomes during cell division, EGFP-Ninein was cloned into the PiggyBac plasmid and transfected into MERVL::tdTomato cells. Positive cells were selected by FACS based on moderate EGFP expression.

To generate the ATM/ATR/CHEK1/CHEK2/PARP-knockdown cell lines, each shRNA oligo was ligated into the pLVX-U6-shRNA-PGK-hygro vector. All constructs were introduced into the 53BP1-mVenus, MERVL::tdTomato, or H2B-mIFP mESC lines using lentiviral transduction. The transduced cells were selected with 150 µg/mL hygromycin for 7–10 days to establish stable cell lines. The knockdown efficiency was verified by qPCR and western blot analysis.

Drug treatment

Drug concentrations: DTT (dithiothreitol, 2 mM), TM (tunicamycin, 10 µM), BTZ(bortezomib, 1 µM), 2-MeOE2 (2-methoxyestradiol, 10 µM), NaCl (200 mM), sucrose (400 mM), PEG (polyethylene glycol, 10.67%), Aph (aphidicolin, 1.25 µM, 2.5 µM, and 5 µM), HU (hydroxyurea, 0.2 mM, 0.4 mM, and 0.8 mM), MMC (mitomycin C, 0.25 µg/mL, 0.5 µg/mL, and 1 µg/mL), ATR inhibitor VE-821 (0.5 µM), ATM inhibitor KU-5593 (10 µM), CHEK1/2 inhibitor debromohymenialdisine (20 µM), and PARP inhibitor PARP-1-IN-3 (1.5 µM). Aph, HU, and MMC treatments were carried out for 8 h, followed by wash-off. Cells were then cultured in fresh culture medium for another 24 h before fixation. DTT, TM, BTZ, 2-MeOE2, NaCl, sucrose, and PEG were introduced for the times shown in the figures. ATMi, ATRi, CHEK1/2i, and PARPi treatments were applied throughout the live-cell imaging.

Live-cell imaging

Cells were seeded on glass-bottom 96-well plates coated with mouse or human laminin for 8–12 h before imaging. Live-cell imaging was performed on a Nikon Ti2-E microscope with a Spectra X light engine (Lumencor) and appropriate filter sets (mIFP: ex 640/30 nm, em 720/60 nm; tdTomato, mCherry, or DsRed2: ex 550/15 nm, em 595/33 nm; GFP or mVenus: ex 475/28 nm, em 519/26 nm). Either a 10× 0.45 NA objective or a 20× 0.75 NA objective was used. Images were acquired with an ORCA-Flash 4.0 V3 CMOS camera (Hamamatsu) at a frequency of 15 min or 20 min per frame. Z-stacks of EGFP-Ninein were captured covering a total depth of 14 µm with a step size of 2 µm. All other images were single-plane acquisitions. Light exposure times were 50–100 ms for Cy5, 30–50 ms for FITC, and 30–50 ms for Cy3, with 50% lamp intensity. Light exposure and imaging frequency were minimized to avoid significant photobleaching and photodamage, while maintaining sufficient temporal resolution for single-cell tracking and signal-to-noise ratio for quantification. During imaging, cells were kept within a dark chamber stably maintained at 37 °C, 5% CO_2, and 95% humidity.

Immunofluorescence (IF) and fixed-cell imaging

For monolayer cell immunostaining, cells seeded on glass-bottom 96-well plates were fixed with 4% PFA, permeabilized with 0.2% Triton X-100 in PBS, blocked with 5% goat serum in 0.1% Triton X-100 (blocking buffer), and incubated with primary antibodies diluted in blocking buffer overnight at 4 °C. Antibodies used were: phospho-histone H2A.X (γH2AX, Ser139) (D7T2V), 1:200; PERK (phospho T980), 1:400; phospho-p53 (Ser15), 1:200; MERVL-Gag, 1:10,000; Nanog (eBioMLC-51), 1:250; Oct3/4, 1:200, Zscan4, 1:15,000; 53BP1, 1:200; Alexa Fluor 488/568/647 secondary antibodies, 1:1000. Most IF experiments were imaged using the same wide-field microscope setup used for live-cell imaging. A laser-scanning confocal microscope (ZEISS LSM 900) was used to confirm the co-localization of γH2AX and 53BP1-mVenus. AP staining was carried out using the Vector Blue AP Substrate Kit following the manufacturer's instructions. Bright-field images were captured with a ZEISS Axio Vert.A1 inverted microscope.

Immunoblotting

Cells were washed once with ice-cold PBS and lysed with RIPA lysis buffer (50 mM Tris-HCl 'pH 7.4', 150 mM NaCl, 0.1% SDS, 1 mM EDTA, 1% Triton X-100, fresh 1× protease inhibitor cocktail). Protein concentration was determined using a BCA protein assay kit according to the manufacturer's instructions. Ten micrograms of protein from each sample was loaded per lane on a 12% SDS-PAGE gel. The samples were transferred onto 0.45-µm PVDF membranes. The membranes were blocked with 5% bovine serum albumin (BSA) in TBST (Tris-buffered saline with 0.1% Tween-20) for 2 h at room temperature, and then incubated with primary antibodies (1:1000 dilution) at 4 °C overnight. Blots were washed four times with TBST (5 min per wash), and then incubated with secondary antibodies (1:5000 dilution) for 1 h at room temperature. After additional washes with TBST (four times, 5 min each), the protein bands were visualized using enhanced chemiluminescence, and images were captured on the Bio-Rad Molecular Imager Gel Doc XR+ .

Decay kinetics of pluripotency rejuvenation

MERVL::DsRed2$^+$ and MERVL::DsRed2$^-$ cells were counted and seeded immediately after FACS sorting. For the next 5 days, cells were fixed at the same time every day with 4% PFA and stored in PBS at 4 °C. IF assays were performed on the fifth day.

Image processing, cell tracking, and signal extraction

Raw images were corrected to extract quantitative information from fluorescence intensity. In brief, dark noise was subtracted from the raw image, followed by correction of illumination bias. Dark noise was measured by averaging 10 snapshots with the light source off. The illumination bias of each fluorescence channel was deduced by averaging the cell-free regions of all images within the channel. The background was then removed using top-hat filtering.

Cells were segmented using the pre-trained model in StarDist,[51] with the nuclear channel as the input image (H2B-mIFP in live-cell imaging and DAPI in fixed-cell imaging). Between frames in which the imaging plate was removed from and placed back into the microscope (for example, during drug addition, medium change, or IF after live-cell imaging), plate jitter was calculated by registering images of the nucleus-stained channel and corrected prior to tracking. Cell tracking was carried out using a local tracking method[52] or EllipTrack.[53] In brief, the local tracking method tracks cells by screening the nearest future neighbors. EllipTrack uses machine-learning techniques to deduce probabilities of cell overlap, cell migration, and mitosis using information on cell morphology and position and constructs tracks that maximize the probability throughout the entire movie using the Viterbi algorithm. The result from this global tracking pipeline was further refined using a local correction module, iteratively swapping every two cell tracks between every two neighboring frames and retaining those swaps that significantly increased the combined probabilities of all tracks. To ensure the accuracy of lineages, we manually verified and corrected all tracks quantified in this study.

The fluorescence intensity of each cell was then extracted from background-removed images as the median intensity of pixels within its nuclear mask (nuclear intensity) or a 4-pixel-wide ring around the nuclear mask (cytoplasmic intensity). Nuclear intensity was used for downstream analysis when the fluorescence of interest was located within nuclei or throughout the entire cell, and cytoplasmic intensity was used when the targeted fluorescence was located exclusively in the cytoplasm.

Single-cell analysis

In time-lapse imaging, MERVL-reporter-negative cells were those that exhibited no fluorescence intensity above background levels. MERVL-reporter-positive cells were classified as 2C-entering, 2C-death, and 2C-survived as follows: '2C-entering cells' refers to cells between the appearance of MERVL::FP (FP refers to both MERVL::GFP and MERVL::tdTomato) and the asymmetric division; '2C-death cells' refers to cells between the asymmetric division and cell death, which often exhibit high MERVL-reporter intensity; and '2C-survived cells' refers to the sister branch of the 2C-death cells, ranging from the asymmetric division to the disappearance of MERVL-reporter fluorescence (Fig. 1j).

In lineage survival analysis, if at least one offspring in a lineage survived, the lineage was considered to have survived; if all offspring in a lineage died, the lineage was considered to have died.

To track the fates of 2C-like cells and visualize the lineage tree of MERVL::GFP$^+$ cells, we tracked MERVL::GFP dynamics for each cell. Robust LOWESS smoothing was applied to MERVL::GFP intensity with a window of 2.5 h to reduce noise. The lineage trees were plotted using in-house MATLAB scripts.

To quantify MERVL::GFP intensity of different subpopulations of mESCs, we extracted the MERVL::GFP intensity for each cell at each frame and calculated the median MERVL::GFP intensity over a cell cycle. For MERVL::GFP$^+$ cells, we included all cell cycles within each dying or living lineage from the point of asymmetric division to cell death (2C-death lineage) or return to the MERVL::GFP$^-$ state (2C-survived lineage).

PIP-FUCCI and H2B reporters were used to determine the boundaries of cell-cycle phases. The M/G1 boundary was recognized by chromosome segregation, indicated by the H2B signal. The G1/S boundary was recognized by the fall of the PIP-FUCCI signal below the background threshold. The S/G2 boundary transition was defined as the time at which the PIP-FUCCI level began to rise, detected using a triangle thresholding method[54] (Supplementary information, Fig. S2b).

To calculate the percentage of MERVL::GFP$^+$ cells for each frame in the exogenous cellular damage movie, the threshold for defining MERVL::GFP$^+$ was as follows: $T = \mu + k \times \sigma$, where μ is the median of all cells in the control condition, σ represents its standard deviation, and k is a constant with a value of 2.7.

To track numbers of 53BP1 foci in 2C asymmetric division lineages, 2C lineage fates were manually verified, and 53BP1 foci were counted manually in S phase.

To track old and new centrosomes in asymmetric divisions that generated two daughters with distinct fates, ninein intensity on centrosomes was examined in prometaphase or metaphase. The centrosome with the higher ninein intensity was defined as the old centrosome.

In all box plots, the center line indicates the median; box limits indicate the upper and lower quartiles; whiskers show 1.5× the interquartile range; and points show outliers.

Numerical data were analyzed in MATLAB and plotted in MATLAB, Origin, or GraphPad.

Comet assay

The different subpopulations of 2C-like cells were sorted using FACS. The comet assay was performed using a Comet Assay Kit, following the manufacturer's instructions. In brief, a cell suspension was prepared at a density of 1000 cells/ µL, mixed with low-melting agarose at a volume ratio of 1:7.5, and then placed in solid normal agarose at 4 °C for 10 min until the agarose solidified. Cells were lysed in cold lysis buffer overnight. DNA was unwound in running buffer (200 mM NaOH and 1 mM EDTA) for 1 h at room temperature, then electrophoresed at 20 V in cold running buffer for 30 min and neutralized with neutralization buffer (0.4 M Tris-HCl, pH 7.5) for 5 min. The slides were imaged on a Nikon Ti2-E microscope after DAPI staining for 5 min in the dark. The assays were analyzed using the OpenComet plugin[55] in ImageJ.[56]

Single-cell RNA sequencing

MERVL::GFP$^+$ and MERVL::GFP$^-$ cells were sorted, and single-cell RNA sequencing libraries were constructed using the Chromium Next GEM Chip G Single Cell Kit following the manufacturer's instructions. The libraries were sequenced on an Illumina HiSeq X Ten instrument to obtain 150-nt paired-end reads. Overall sequence quality was examined using FastQC (v0.11.2), and adapter sequences were clipped using Trim Galore (v0.6.4). The reads were mapped to the mouse genome (mm10), and a count matrix was generated using STAR (v2.7.6a).[57] Low-quality cells were filtered out using a gene-number threshold of 3000. Dimensionality reduction was carried out on the count matrix using principal component analysis, followed by clustering and visualization using uniform manifold approximation and projection (UMAP). Differentially expressed genes were analyzed using the Python package Scanpy (v1.8.1) with the function 'rank_genes_groups'.[58] Genes showing an expression change > 2-fold with an adjusted *P*-value < 0.05 were considered differentially expressed. A list of p53 transcriptional target genes was compiled from a previous global run-on sequencing (GRO-seq) study in human cells[59] and mapped to their mouse homologs using biomaRt (v2.50.1).[60] Volcano plots were generated using the seaborn package (v0.11.0),[61] and UMAPs were labeled using the Scanpy package. The NCBI IDs of marker gene sequences are *Zscan4c* (245109), *Ddit4l* (73284), *Nanog* (71950), *Sox2* (20674), and *Pou5f1* (18999). Raw sequencing data have been deposited in the GEO database under accession number GSE289323.

Bulk RNA sequencing

MERVL::DsRed2$^+$ and MERVL::DsRed2$^-$ cells were sorted by FACS and lysed in TRIzol reagent for RNA extraction. Three biological replicates were collected on different dates. Library construction and sequencing were performed by the China National Gene Bank. Libraries were constructed based on the DNBSEQ platform. In brief, after sample quality control, the mRNA was hybridized with an oligo (dT) probe and captured with magnetic beads. The mRNA was then reverse-transcribed to first-strand cDNA, which was used as a template for second-strand DNA synthesis. A dTTP-tailed adapter was ligated to both ends of the dsDNA fragments. The ligation product was amplified by PCR and circularized to obtain a single-stranded circular (ssCir) library, which was then amplified by rolling circle amplification to generate DNA nanoballs (DNBs). The DNBs were then loaded into a flowcell and sequenced on the DNBSEQ platform to obtain 150-bp paired-end reads. Sequence quality was examined using FastQC (v0.12.1), and low-quality bases were removed using Trimmomatic (v0.39). The reads were aligned to the mouse genome (GRCm39) using STAR (v2.7.11b). Alignment was accepted if the ratio of mismatches to mapped length was ≤ 0.04. Mapped fragments were counted using RSEM (v1.3.3). Differential expression analysis was performed using DESeq2 (v1.45.3) in R Studio (v4.4.1). Genes with $\log_2$ (fold change) > 0.5 and adjusted *P*-value < 0.05 were considered to be differentially expressed between the two cell populations. The list of pluripotency genes was obtained from Shen et al. [62] Volcano plots were generated using the tinyarray package (v2.4.2). Raw sequencing data have been deposited in the GEO database under accession number GSE287152.

Clone assay

Cells were plated in 6-well cell culture plates at a density of 600 cells per well. The cells were cultured under routine culture conditions for 5 days, with the medium changed every two days. On day 5, the cells were fixed with 4% PFA, followed by AP staining. The numbers of AP^+ clones were counted manually in Fiji.

Chimera assay

Six- to eight-week-old female mice were superovulated by injection of 5–6 IU of pregnant mare serum gonadotrophin (PMSG). Forty-six to forty-eight h after PMSG injection, 5–6 IU of human chorionic gonadotrophin (hCG) was administered. Superovulated female mice were set up for mating with ICR male mice. About 16–18 h later, mouse zygotes were isolated in M2 medium, and cumulus cells were removed with hyaluronidase. All embryos were then cultured in KSOM medium at 37 °C under 5% CO_2 in air under mineral oil. Approximately 6–8 FACS-selected $DsRed2^-$ or $DsRed2^+$ mESCs were injected into each E3.5 blastocyst. Injected embryos were then rested in KSOM medium. The next day, around 30 injected E4.5 embryos were transferred into both oviducts of a D0.5 pseudopregnant ICR mouse. Dissection was performed at E9.5. Chimeric conceptuses were observed using a Leica M165 FC fluorescent stereo microscope, and the manual scoring of chimeric embryos was blinded. For FACS quantification, cells were dissociated using a mixture of 0.05% trypsin:TrypLE (1:1) and neutralized in MEF medium (high glucose DMEM, 4 mM L-glutamine, 10% fetal bovine serum, 1 U/mL penicillin, 1 mg/mL streptomycin). The cells were then centrifuged, and the pellets were resuspended in 2% knockout serum in PBS. After filtration through a 35-µm strainer cap, the cells were analyzed on a BD LSR Fortessa X-20 flow cytometer. Data were analyzed using FlowJo 10 software.

Blastocyst immunostaining

Approximately three FACS-selected $MERVL::GFP^-$, MERVL::GFP-low, or MERVL::GFP-high mESCs were injected into each E2.5 blastocyst. The injected embryos were then cultured in KSOM medium. Three days later, E5.5 embryos were fixed with 4% formaldehyde for 30 min at room temperature. Samples were then washed three times for 5 min each with 0.1% Triton X-100 in PBS. After permeabilization with 0.3% Triton X-100 for 30 min, the samples were blocked with 3% donkey serum, 1% BSA, and 0.1% Triton X-100 in PBS for 2 h, and then incubated with primary antibodies at 4 °C overnight. The next day, embryos were washed four times with 0.1% Triton X-100 for 5 min each, incubated with fluorescently labeled secondary antibodies for 2 h, and stained with DAPI for 5 min at room temperature. Antibodies used: CDX2 (D7T2V)/SOX2 (Btjce)/mCherry, 1:200; Alexa Fluor 488/568/647 secondary antibodies, 1:500. Images were acquired using a Carl Zeiss LSM 800 confocal microscope and processed using ZEN software. Chimeric efficiency was calculated as the percentage of $mCherry^+$ blastocysts.

Karyotype analysis

Karyotype analysis was performed by the karyotyping facility at Guangzhou Institutes of Biomedicine and Health. In brief, mESCs were arrested at prometaphase with 200 ng/mL colchicine for 1 h at 37 °C and collected in pre-warmed hypotonic KCl solution. After incubation for 30 min at 37 °C, the cells were fixed with methanol and acetic acid (3:1) and dropped onto pre-cooled slides. Chromosomes were stained with Giemsa solution, imaged using a ZEISS Axio Imager 2 Microscope, and analyzed with Ikaros karyotyping software. A minimum of 20 prometaphase spreads were analyzed.

Quantification and statistical analysis

Imaging data were quantified in MATLAB or ImageJ as described above. Processed data are presented as the means ± standard error of the mean (SEM), median ± quantile (box plots), or single-cell density distributions (density plots), as indicated in the figure legends. Sample size and replicate numbers are indicated in the figure legends. Statistical analyses are indicated in the figure legends and main text ($****P \leq 0.0001$, $***P \leq 0.001$, $**P \leq 0.01$, $*P \leq 0.05$; ns, $P > 0.05$).

REFERENCES

1. Weismann, A. *The Germ-Plasm: A Theory of Heredity* (W. Scott, London, 1893).
2. Kirkwood, T. B. L. Evolution of ageing. *Nature* **270**, 301–304 (1977).
3. López-Otín, C., Blasco, M. A., Partridge, L., Serrano, M. & Kroemer, G. Hallmarks of aging: An expanding universe. *Cell* **186**, 243–278 (2023).
4. Evans, M. J. & Kaufman, M. H. Establishment in culture of pluripotential cells from mouse embryos. *Nature* **292**, 154–156 (1981).
5. Suda, Y., Suzuki, M., Ikawa, Y. & Aizawa, S. Mouse embryonic stem cells exhibit indefinite proliferative potential. *J. Cell. Physiol.* **133**, 197–201 (1987).
6. Zalzman, M. et al. Zscan4 regulates telomere elongation and genomic stability in ES cells. *Nature* **464**, 858–863 (2010).
7. Niida, H. et al. Severe growth defect in mouse cells lacking the telomerase RNA component. *Nat. Genet.* **19**, 203–206 (1998).
8. Markiewicz-Potoczny, M. et al. TRF2-mediated telomere protection is dispensable in pluripotent stem cells. *Nature* **589**, 110–115 (2021).
9. Macfarlan, T. S. et al. Embryonic stem cell potency fluctuates with endogenous retrovirus activity. *Nature* **487**, 57–63 (2012).
10. Du, Z. et al. The totipotent 2C-like state safeguards genomic stability of mouse embryonic stem cells. *J. Cell. Physiol.* **239**, e31337 (2024).
11. Amano, T. et al. Zscan4 restores the developmental potency of embryonic stem cells. *Nat. Commun.* **4**, 1966 (2013).
12. Olbrich, T. et al. CTCF is a barrier for 2C-like reprogramming. *Nat. Commun.* **12**, 4856 (2021).
13. Grow, E. J. et al. p53 convergently activates Dux/DUX4 in embryonic stem cells and in facioscapulohumeral muscular dystrophy cell models. *Nat. Genet.* **53**, 1207–1220 (2021).
14. Nakatani, T. et al. DNA replication fork speed underlies cell fate changes and promotes reprogramming. *Nat. Genet.* **54**, 318–327 (2022).
15. Jia, S., Wen, X., Zhu, M. & Fu, X. The pluripotent-to-totipotent state transition in mESCs activates the intrinsic apoptotic pathway through DUX-induced DNA replication stress. *Cell. Mol. Life Sci.* **81**, 440 (2024).
16. Nakai-Futatsugi, Y. & Niwa, H. Zscan4 is activated after telomere shortening in mouse embryonic stem cells. *Stem Cell Rep.* **6**, 483 (2016).
17. Yu, D. et al. A naturally monomeric infrared fluorescent protein for protein labeling in vivo. *Nat. Methods* **12**, 763–765 (2015).
18. Ying, Q. L. et al. The ground state of embryonic stem cell self-renewal. *Nature* **453**, 519–523 (2008).
19. Hu, Y. et al. Induction of mouse totipotent stem cells by a defined chemical cocktail. *Nature* **617**, 792–797 (2023).
20. Taubenschmid-Stowers, J. et al. 8C-like cells capture the human zygotic genome activation program in vitro. *Cell Stem Cell* **29**, 449–459.e6 (2022).
21. Mazid, M. A. et al. Rolling back human pluripotent stem cells to an eight-cell embryo-like stage. *Nature* **605**, 315–324 (2022).
22. Wang, Y. et al. Unique molecular events during reprogramming of human somatic cells to induced pluripotent stem cells (iPSCs) at naïve state. *Elife* **7**, e29518 (2018).
23. Mortimer, R. K. & Johnston, J. R. Life span of individual yeast cells. *Nature* **183**, 1751–1752 (1959).
24. Aguilaniu, H., Gustafsson, L., Rigoulet, M. & Nyström, T. Asymmetric inheritance of oxidatively damaged proteins during cytokinesis. *Nature* **299**, 1751–1753 (2003).
25. Shcheprova, Z., Baldi, S., Frei, S. B., Gonnet, G. & Barral, Y. A mechanism for asymmetric segregation of age during yeast budding. *Nature* **454**, 728–734 (2008).
26. Li, Y. et al. A programmable fate decision landscape underlies single-cell aging in yeast. *Science* **369**, 325–329 (2020).
27. Jiang, Z., Generoso, S. F., Badia, M., Payer, B. & Carey, L. B. A conserved expression signature predicts growth rate and reveals cell & lineage-specific differences. *PLoS Comput. Biol.* **17**, e1009582 (2021).
28. Liu, J. et al. The RNA m6A reader YTHDC1 silences retrotransposons and guards ES cell identity. *Nature* **591**, 322–326 (2021).
29. Zhu, Y. et al. Cell cycle heterogeneity directs spontaneous 2C state entry and exit in mouse embryonic stem cells. *Stem Cell Rep.* **16**, 2659–2673 (2021).
30. Grant, G. D., Kedziora, K. M., Limas, J. C., Cook, J. G. & Purvis, J. E. Accurate delineation of cell cycle phase transitions in living cells with PIP-FUCCI. *Cell Cycle* **17**, 2496–2516 (2018).
31. Sedelnikova, O. A. et al. Senescing human cells and ageing mice accumulate DNA lesions with unrepairable double-strand breaks. *Nat. Cell Biol.* **6**, 168–170 (2004).
32. Canat, A. & Atilla, D. & Torres-Padilla, M. Hyperosmotic stress induces 2-cell-like cells through ROS and ATR signaling. *EMBO Rep.* **24**, e56194 (2023).
33. Iwabuchi, K. et al. Potential role for 53BP1 in DNA end-joining repair through direct interaction with DNA. *J. Biol. Chem.* **278**, 36487–36495 (2003).
34. Banáth, J. P. et al. Explanation for excessive DNA single-strand breaks and endogenous repair foci in pluripotent mouse embryonic stem cells. *Exp. Cell Res.* **315**, 1505–1520 (2009).
35. Ahuja, A. K. et al. A short G1 phase imposes constitutive replication stress and fork remodelling in mouse embryonic stem cells. *Nat. Commun.* **7**, 10660 (2016).
36. Turinetto, V. et al. High basal γH2AX levels sustain self-renewal of mouse embryonic and induced pluripotent stem cells. *Stem Cells* **30**, 1414–1423 (2012).

37. Byers, B. Cytology of the yeast life cycle. In *The Molecular Biology of the Yeast* Saccharomyces: *Life Cycle and Inheritance* (eds Strathern, J. N., Jones, E. W. & Broach, J. R.) 59–96 (Cold Spring Harbor Laboratory, 1981).
38. Bouckson-Castaing, V. et al. Molecular characterisation of ninein, a new coiled-coil protein of the centrosome. *J. Cell Sci.* **109**, 179–190 (1996).
39. Khmelinskii, A. et al. Tandem fluorescent protein timers for in vivo analysis of protein dynamics. *Nat. Biotechnol.* **30**, 708–714 (2012).
40. He, L., Binari, R., Huang, J., Falo-Sanjuan, J. & Perrimon, N. In vivo study of gene expression with an enhanced dual-color fluorescent transcriptional timer. *Elife* **8**, e46181 (2019).
41. Stewart, E. J., Madden, R., Paul, G. & Taddei, F. Aging and death in an organism that reproduces by morphologically symmetric division. *PLoS Biol.* **3**, e45 (2005).
42. Greider, C. W. & Blackburn, E. H. Identification of a specific telomere terminal transferase activity in tetrahymena extracts. *Cell* **43**, 405–413 (1985).
43. Bryan, T. M., Englezou, A., Dalla-Pozza, L., Dunham, M. A. & Reddel, R. R. Evidence for an alternative mechanism for maintaining telomere length in human tumors and tumor-derived cell lines. *Nat. Med.* **3**, 1271–1274 (1997).
44. Chew, G. L. et al. DUX4 suppresses MHC class I to promote cancer immune evasion and resistance to checkpoint blockade. *Devel. Cell* **50**, 658–671.e7 (2019).
45. Smith, A. A. et al. DUX4 expression in cancer induces a metastable early embryonic totipotent program. *Cell Rep.* **42**, 113114 (2023).
46. Portney, B. A. et al. ZSCAN4 facilitates chromatin remodeling and promotes the cancer stem cell phenotype. *Oncogene* **39**, 4970–4982 (2020).
47. Li, X. et al. Generation of Destabilized Green Fluorescent Protein as a Transcription Reporter. *J. Biol. Chem.* **273**, 34970–34975 (1998).
48. Mok, M. T. S. & Henderson, B. R. The in vivo dynamic interplay of MDC1 and 53BP1 at DNA damage-induced nuclear foci. *Int. J. Biochem. Cell Biol.* **44**, 1398–1409 (2012).
49. Falco, G. et al. Zscan4: A novel gene expressed exclusively in late 2-cell embryos and embryonic stem cells. *Dev. Biol.* **307**, 539–550 (2007).
50. Delgehyr, N., Sillibourne, J. & Bornens, M. Microtubule nucleation and anchoring at the centrosome are independent processes linked by ninein function. *J. Cell Sci.* **118**, 1565–1575 (2005).
51. Weigert, M. & Schmidt, U. Nuclei instance segmentation and classification in histopathology images with stardist. In *2022 IEEE International Symposium on Biomedical Imaging Challenges (ISBIC)*, 1–4 (2022).
52. Cappell, S. D., Chung, M., Jaimovich, A., Spencer, S. L. & Meyer, T. Irreversible APC(Cdh1) inactivation underlies the point of no return for cell-cycle entry. *Cell* **166**, 167–180 (2016).
53. Tian, C., Yang, C. & Spencer, S. L. EllipTrack: A global-local cell-tracking pipeline for 2D fluorescence time-lapse microscopy. *Cell Rep.* **32**, 107984 (2020).
54. Zack, G. W., Rogers, W. E. & Latt, S. A. Automatic measurement of sister chromatid exchange frequency. *J. Histochem. Cytochem.* **25**, 741–753 (1977).
55. Gyori, B. M., Venkatachalam, G., Thiagarajan, P. S., Hsu, D. & Clement, M. V. OpenComet: An automated tool for comet assay image analysis. *Redox Biol.* **2**, 457–465 (2014).
56. Schindelin, J. et al. Fiji: an open-source platform for biological-image analysis. *Nat. Methods* **9**, 676–682 (2012).
57. Dobin, A. et al. STAR: Ultrafast universal RNA-seq aligner. *Bioinformatics* **29**, 15–21 (2013).
58. Wolf, F. A., Angerer, P. & Theis, F. J. SCANPY: large-scale single-cell gene expression data analysis. *Genome Biol.* **19**, 15 (2018).
59. Allen, M. A. et al. Global analysis of p53-regulated transcription identifies its direct targets and unexpected regulatory mechanisms. *Elife* **3**, e02200 (2014).
60. Durinck, S. et al. BioMart and Bioconductor: a powerful link between biological databases and microarray data analysis. *Bioinformatics* **21**, 3439–3440 (2005).
61. Waskom, M. seaborn: statistical data visualization. *J. Open Source Softw.* **6**, 3021 (2021).
62. Shen, H. et al. Mouse totipotent stem cells captured and maintained through spliceosomal repression. *Cell* **184**, 2843–2859.e20 (2021).

ACKNOWLEDGEMENTS

We thank Dr. Yangming Wang for the *Zscan4* promoter plasmid, Dr. Miguel A. Esteban for the TPRX1-GFP cell line, Dr. Ian Chambers for the E14 TG2a cells, Drs. José Silva and Sabrina Spencer for insightful comments on the manuscript, Ms. Chan Feng for manually verifying ESC lineages from cell tracking data, and the Min Lab and all members of CCLA for general discussions and assistance. This work is supported by National Natural Science Foundation of China (32170732, 32300665), Pearl River Talent Recruitment Program (2021ZT09Y233), Major Project of Guangzhou National Laboratory (GZNL2025C02017, GZNL2024A02005, GZNL2023A02005) and Guangdong Basic and Applied Basic Research Foundation Special Projects-Guangdong-Guangzhou Joint Funds (2022A1515110199).

AUTHOR CONTRIBUTIONS

M.Z. and M.M. designed the study. A.G., J.L., G.P., J.C., and G.W. developed the experimental methodology. X.W., H.F., Q.S., B.H., Z.X., X.Z., C.D., L.P., M.D.Z., and T.P. performed the experiments and collected the data. X.W., H.F., Q.S., Z.X., and X.Z. analyzed the data and prepared the figures. A.G., M.Z., and M.M. provided financial support. M.Z. and M.M. managed the project. Z.Z., M.Z., and M.M. supervised the study. X.W., H.F., Q.S., Z.X., and M.M. wrote the original draft of the manuscript. X.W., H.F., Q.S., B.H., J.L., M.Z., and M.M. revised and edited the manuscript. All authors contributed to the discussion of the study and to the interpretation of the results.

COMPETING INTERESTS

The authors declare no competing interests.

ADDITIONAL INFORMATION

Supplementary information The online version contains supplementary material available at https://doi.org/10.1038/s41422-026-01221-z.

Correspondence and requests for materials should be addressed to Man Zhang or Mingwei Min.

Reprints and permission information is available at http://www.nature.com/reprints